Physics of Fluids

# The effects of caudal fin's bending stiffness on a self-propelled carangiform swimmer

Cite as: Phys. Fluids **34**, 041901 (2022); https://doi.org/10.1063/5.0089082
Submitted: 22 February 2022 • Accepted: 16 March 2022 • Published Online: 04 April 2022

**Buchen Wu** (吴步晨), **Chang Shu** (舒昌), **HsuChew Lee, et al.**

Physics of Fluids ARTICLE scitation.org/journal/phf

# The effects of caudal fin's bending stiffness on a self-propelled carangiform swimmer

Cite as: Phys. Fluids **34**, 041901 (2022); doi: 10.1063/5.0089082
Submitted: 22 February 2022 · Accepted: 16 March 2022 ·
Published Online: 4 April 2022



Buchen Wu (吴步晨),[1,2] Chang Shu (舒昌),[2,a)] HsuChew Lee,[1,3] and Minping Wan (万敏平)[1,3,a)]

## AFFILIATIONS

[1]Guangdong Provincial Key Laboratory of Turbulence Research and Applications, Department of Mechanics and Aerospace Engineering, Southern University of Science and Technology, Shenzhen, Guangdong 518055, China
[2]Department of Mechanical Engineering, National University of Singapore, 10 Kent Ridge Crescent, Singapore 119260, Singapore
[3]Guangdong-Hong Kong-Macao Joint Laboratory for Data-Driven Fluid Mechanics and Engineering Applications, Southern University of Science and Technology, Shenzhen 518055, China

[a)]**Authors to whom correspondence should be addressed:** mpeshuc@nus.edu.sg and wanmp@sustech.edu.cn

## ABSTRACT

The hydrodynamic performance of a self-propelled carangiform swimmer with a flexible caudal fin in the absence of a free stream is numerically investigated, where the fin's dimensionless bending stiffness varies from $10^{-3}$ to 150. It reveals that large flexibility of the caudal fin has a negative impact on the propulsion and moderate rigidity is found to increase the hydrodynamic performance. Two different vortex configurations are observed at low and high bending stiffnesses: (i) reverse Bénard–von Kármán (rBvK) vortex configuration and (ii) deflected reverse Bénard–von Kármán wake with the secondary vortex street, respectively. With the increase in bending stiffness, the thrust-producing part switches from the swimmer body to the caudal fin corresponding to the switch of the vortex configuration. Furthermore, the thrust and drag productions are examined. As the bending stiffness increases, the "active portion" of the caudal fin provides more kinetic energy to the wake flow. It is found that the deflected rBvK is induced by the vortical strength imbalance of two adjacent vortices, and the secondary vortex street is formed by the large strain between the primary vortex and the secondary vortex street. Meanwhile, the dynamic mode decomposition analysis indicates that the dominant mode of the dynamic flow field is the excited frequency resonant mode and the inherent frequency of the secondary vortex street is the same as the undulatory frequency. These results shed new light onto the role of the flexible caudal fin in self-propelled biological systems and may provide some inspirations to autonomous underwater vehicle design.



## I. INTRODUCTION

Autonomous underwater vehicles (AUVs) have received a considerable amount of attention due to their wide range of applications, but conventional propulsive mechanisms have severe limitations, especially in complex marine environments. Hence, researchers have focused on a new form of AUVs that is based on aquatic animals' swimming and maneuvering capabilities,[1,2] where they have far superior performances in terms of speed and efficiency. Most of the natural swimmers propel themselves through undulation motion,[3–5] which is a wave motion along the swimmer's body controlling the surrounding flow plastered to its surface. The common undulatory profiles of natural swimmers are anguilliform, carangiform, subcarangiform, and thunniform,[6,7] and the present work focuses solely on carangiform motion. General fish swimming patterns include body and/or caudal fin (BCF) and median and/or paired fin (MPF) modes.[8–10] The BCF modes are mostly adopted by carangiform swimmers, where the propulsive process is achieved through the swimmer swinging its body from side to side to drive the caudal fin that interacts with the surrounding flows. Understanding how the BCF system interacts with surrounding flow is important to further improve the AUV's efficiency.

Several studies[11–13] have demonstrated that the flexible part plays an important role in natural propulsion, i.e., propulsive speed and efficiency enhancement, enhancing wake symmetry preserving ability, which triggers many investigations onto the BCF system. Generally, studies on BCF systems can be divided into two groups. The first group of researchers simplifies the BCF system as a flapping foil with the flexible plate,[13–19] and the second group of researchers adopts an undulatory foil with various caudal fins[8,20–27] to simulate the BCF system. Heathcote and Gursul[14] found that the vortical strength of the leading-edge vortex (LEV), Strouhal number (St), and pitching phase angle is related to the propulsive efficiency of the flexible flapping foil.

Dewey *et al.*[15] reported that the flapping foil with the flexible panel can generate higher thrust and propulsive efficiency than those with rigid panels and the maximum propulsive efficiency is dependent on two criteria: (i) optimal range of St and (ii) the specific flapping frequency resonant to natural frequency of the system. Shinde and Arakeri[16] found that, in the absence of a free stream, the flexible flap can effectively preserve the wake symmetry of the foil-flexible flap system and the coherent jet structure is associated with the St. In their subsequent work, they[18] reported that the flexible flap is composed of an active portion and a "passive portion." The active portion promotes the wake flow momentum and kinetic energy; meanwhile, the passive portion is related to the vortex shedding position. David *et al.*[17] reported that the efficiency of the tethered pitching foil with the flexible flap can achieve up to three times with dimensionless bending stiffness $R^* \approx 0.01$ and the system with $R^* \approx 8$ generates the maximum thrust. He *et al.*[28] found that the vibration amplitude with the Strouhal number $St_A$ is positively proportional to the Reynolds number and the range of wake width with the Strouhal number is $St_w \in [0.14, 0.21]$, indicating that the wake flow is a bluff-body wake.

Among different undulatory profiles of the natural swimmer, the undulatory swimmer with the caudal fin, which couples the swimmer movement with the interaction of the caudal fin and surrounding flow, has recently received much attention. Liu *et al.*[20,21] investigated the hydrodynamic performance of a tethered wave foil with a rigid plate (the joint point is modeled by a torsional spring that allows the adjustment of the flexibility of the caudal fin) and found that the joint bending stiffness and the caudal fin's length play important roles in fish swimming. Tian *et al.*[8] adopted a tethered carangiform swimmer with the two-dimensional flexible plate as the BCF system and found that the properties of the caudal fin significantly affect the hydrodynamic performance. Bergmann *et al.*[23] modeled the caudal fin as a series of rigid struts connected by elastic links and reported that the optimal efficiency can be achieved at moderate flexibility and that either excessive bending stiffness or compliance has an adverse effect on the propulsion. Kancharala and Philen[22] numerically and experimentally investigated the effect of joint flexibility on the propulsive performance and adopted the nonlinear Euler–Bernoulli beam theory to model the dynamic behavior of the caudal fin, where their numerical results are consistent with the experimental results. Gao and Triantafyllou[25] and Zhao and Dou[24] treated the flapping foil as an independent caudal fin, following the fish-like undulatory foil, and found that the independent foil can effectively promote the propulsive efficiency.

In nature, the biological BCF system can freely propel in the omni-direction, but most studies that are available in the literature placed their focus on the tethered BCF system, constraining it at a fixed position. Moreover, to the best of the authors' knowledge, the investigations about the effects of the caudal fin on the hydrodynamic performance of the self-propelled BCF system remain sparse. In the present work, the hydrodynamic performances of an unconstrained carangiform swimmer with the flexible caudal fin are systematically studied to unravel the mechanism on how a natural BCF system gains propulsive advantages from the passive deformation of the caudal fin to achieve better propulsion. In Sec. II, the problem description and governing equations are described. Numerical methods and validations are provided in Sec. III, and numerical results and analysis are provided in Sec. IV followed by conclusions in Sec. V.

## II. PHYSICAL PROBLEM AND MATHEMATICAL FORMULATION

The schematic view of the carangiform swimmer with the flexible caudal fin is shown in Fig. 1. In this study, the NACA 0012 foil is employed to emulate the carangiform swimmer's shape and a prescribed undulatory motion is imposed on the swimmer's backbone mimicking the natural swimmer propulsion. The amplitude profile $A(x_s)$ of the carangiform swimmer can be written as

$$\mathrm{A}(x_s) = \mathrm{C}_0 - \mathrm{C}_1 x_s + \mathrm{C}_2 (x_s)^2, \quad x_s \in [0, c], \tag{1}$$

where $x_s$ is the local coordinate of swimmer's surface point, $C_0$, $C_1$, and $C_2$ are the propulsive coefficients obtained from the experimental data of a steadily swimming saithe fish, and they are set as 0.02, 0.0825, and 0.1625, respectively, in this study.

The prescribed lateral displacement of the flexible backbone is determined through the following time-dependent undulatory governing equation:

$$y_s(x_s, \mathrm{t}) = \mathrm{A}(x_s) \cos(\mathrm{k}x_s - 2\pi \mathrm{ft} + \vartheta), \tag{2}$$

where $\mathrm{k} = 2\pi/\lambda$ is the wave number and $\lambda$ denotes the wavelength, f is the undulatory frequency, $\vartheta$ is the phase angle of the carangiform swimmer, and $y_s$ represents the local lateral displacement of the backbone. In this study, the wavelength $\lambda$ is set to be identical to body length and the phase angle $\vartheta$ is defined as zero. Hence, Eq. (2) can be rewritten as

$$y_s(x_s, \mathrm{t}) = \mathrm{A}(x_s) \cos(2\pi(x_s - \mathrm{ft})). \tag{3}$$

In addition, the locomotion of the carangiform swimmer is governed by Newton's second law as follows:

$$m \frac{\mathrm{d}^2 \boldsymbol{\Psi}}{\mathrm{d}t^2} = \boldsymbol{F}_H, \tag{4}$$

where $\boldsymbol{\Psi}$ denotes the position of the swimmer's mass center in both horizontal and vertical directions and $\boldsymbol{F}_H = \boldsymbol{F}_{foil} + \boldsymbol{F}_{fin}$ is the total hydrodynamic force exerted on the BCF system by surrounding flows. $m = m_{foil} + m_{fin}$ denotes the mass of the swimmer, where $m_{foil} = \rho_s S$ in which $\rho_s$ is the area density of the swimmer, and $S$ denotes the area of the swimmer. In this work, the area density of the foil $\rho_s$ is equal to

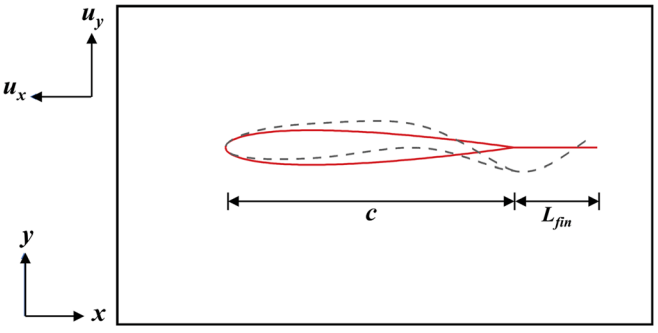


**FIG. 1.** Schematic view of the simplified carangiform swimmer with the caudal fin. $c$ is the chord length, and $L_{fin}$ is the length of the flexible caudal fin. The red line denotes that the swimmer is composed of NACA 0012 with a flexible plate, and the dashed gray line shows the instantaneous propulsive shape.

the fluid density because the mass ratio is not the focus of the present work and $S$ is specified as 0.086 21 m$^2$.[29]

To quantify the hydrodynamic performance of the swimmer, the time-averaged propulsive speeds along the horizontal direction and vertical direction are computed as $u_x = \frac{1}{T}\int_0^T u_{xi}dt$ and $u_y = \frac{1}{T}\int_0^T u_{yi}dt$, respectively.

To further evaluate the hydrodynamic performance of the BCF system, the power consumption to generate the vertical oscillation of the swimmer is defined as

$$P = -\oint_s f_{sy}u_{sy}ds, \tag{5}$$

where $f_{sy}$ denotes the lateral hydrodynamic force per unit length on the swimmer body and $u_{sy}$ is the corresponding instantaneous lateral velocity on the swimmer surface. The propulsive efficiency of the BCF system is the ratio of the averaged kinetic energy obtained from the undulatory motion ($\overline{E}_k = \frac{1}{2}mu_x^2$) to the averaged input power ($W = \overline{P}T$), and it can be expressed as $\eta = \overline{E}_k/W$.

To simulate the incompressible flow, the Navier–Stokes (NS) equations of mass and momentum conservation are adopted,

$$\frac{\partial \mathbf{u}}{\partial t} + \mathbf{u}\cdot\nabla\mathbf{u} = -\frac{1}{\rho_f}\nabla p + \nu\cdot\nabla^2\mathbf{u} + \mathbf{f}, \tag{6}$$

$$\nabla\cdot\mathbf{u} = 0, \tag{7}$$

where $\rho_f$ is the fluid density, $\mathbf{u}$ denotes the flow velocity, $\nu$ is the kinematic viscosity, p is the pressure, and $\mathbf{f}$ is the force generated by the solid system exerting on the fluid, which is resolved by the immersed boundary method.[30] The Reynolds number is defined as $\mathrm{Re} = U_{ref}L_{ref}/\nu$, where $U_{ref}$ is the reference velocity and the characteristic length is set as $L_{ref} = c + L_{fin}$.

The structural governing equation[31,32] of the flexible caudal fin can be expressed as follows:

$$\rho_s\frac{\partial^2\boldsymbol{X}}{\partial t^2} = \frac{\partial}{\partial s}\left(T\frac{\partial\boldsymbol{X}}{\partial s}\right) - \frac{\partial^2}{\partial s^2}\left(EI\frac{\partial^2\boldsymbol{X}}{\partial s^2}\right) + \boldsymbol{F}_{fin}, \tag{8}$$

where $\rho_s$ is the linear density of the flexible caudal fin and $s$ denotes the Lagrangian coordinate along the caudal fin. $\boldsymbol{X}(s,t) = (x(s,t), y(s,t))$ is the local position of solid points along the flexible caudal fin, $T$ is the tensile stress, $EI$ is the bending stiffness, and $\boldsymbol{F}_{fin}$ is the hydrodynamic force applied on the caudal fin by the surrounding flow.

Since the leading edge of the caudal fin and wave foil are connected, the position $\boldsymbol{X}$, velocity $\boldsymbol{U}$, and the first-order derivative $\partial\boldsymbol{X}/\partial s$ of the fin's fixed end should be updated according to the physical information of wave foil.

At the leading edge of the caudal fin,

$$\boldsymbol{X} = \boldsymbol{X}_{foil\ end}, \tag{9}$$

$$\boldsymbol{U} = \boldsymbol{U}_{foil\ end}, \tag{10}$$

$$\frac{\partial\boldsymbol{X}}{\partial s} = (\cos\alpha(t), \sin\alpha(t)), \tag{11}$$

where $\alpha(t) = \frac{\partial y_s}{\partial x_s}\big|_{x_s=c} = -2\pi A(c)\sin(2\pi(c-ft))$ is the deflection angle at the end of wave foil.

At the trailing edge of the caudal fin,

$$\frac{\partial^2\boldsymbol{X}}{\partial s^2} = 0, \tag{12}$$

$$\frac{\partial^3\boldsymbol{X}}{\partial s^3} = 0, \tag{13}$$

$$T = 0. \tag{14}$$

To normalize Eq. (8), the mass ratio between the fin and the fluid is defined as $\beta = \rho_s/(\rho_f L_{fin})$. The tensile stress is obtained by $T = \mathrm{K_s}\left(\left|\frac{\partial\boldsymbol{X}}{\partial s}\right| - 1\right)$ with a constant stretching coefficient $\mathrm{K_s}$, and the dimensionless stretching coefficient is defined as $k_s = \mathrm{K_s}/\rho_s U_{ref}^2$. The dimensionless bending stiffness is given as $k_b = EI/\rho_s U_{ref}^2 L_{fin}^2$.

## III. NUMERICAL VALIDATION OF THE PRESENT SOLVER

The governing equations of the fluid–structure coupling problem are solved by an immersed boundary-lattice Boltzmann flux solver (LBFS) for surrounding flows and a finite element method for the dynamic response of the caudal fin. The lattice Boltzmann flux solver (LBFS)[33] has been extensively used to simulate incompressible viscous flows, and the explicit velocity correction-based immersed boundary method[30,34] is adopted to resolve the interaction between the solid system and the fluid. The LBFS use the finite volume method to discretize the flow field. Details about the flow solver and immersed boundary method can be found in the literature studies.[30,33,34] The structural equation for the caudal fin is discretized by a finite difference method proposed by Ma *et al.*[32] In addition, the methodology for fluid–structure coupling follows previous studies, and details about the numerical details can be found in the literature studies.[32,35–38]

Three test cases are selected to vigorously test and validate the flexible structure–fluid coupling solver employed in this study, namely, a two-dimensional (2D) flapping filament, a 2D inverted flapping flag, and a tethered wave foil in uniform flow. Figure 2(a) shows the simulation of the flapping filament with the simply supported condition in the uniform flow with identical simulation parameters ($\mathrm{Re} = 165$, $k_s = 2\times10^{-3}$, $k_b = 1\times10^{-3}$, and $\beta = 0.3$) used by Yuan *et al.*,[39] where the numerical results obtained in the present study are in excellent agreement with those in Yuan *et al.*[39] The numerical results for the inverted flapping flag with the built-in support condition in the uniform flow with the same parameters ($\mathrm{Re} = 200$, $k_s = 5\times10^{-3}$,

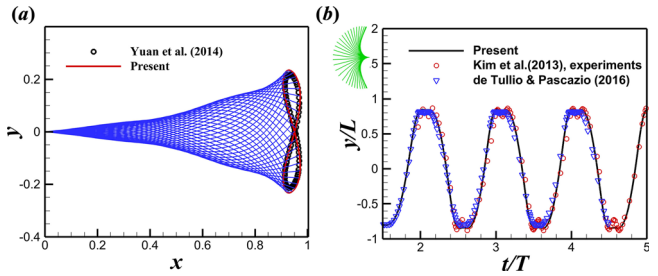


**FIG. 2.** (*a*) The comparison of periodic trailing edge position in the case of ($\mathrm{Re} = 165$, $k_s = 2\times10^{-3}$, $k_b = 1\times10^{-3}$, and $\beta = 0.3$), and the blue lines denote the flapping profile. (*b*) The comparison of time histories of the transverse displacements of an inverted flexible flag in the case of ($\mathrm{Re} = 200$, $k_s = 5\times10^{-3}$, $k_b = 0.1$, $\beta = 2.9$), and the green lines denote the flapping profile.

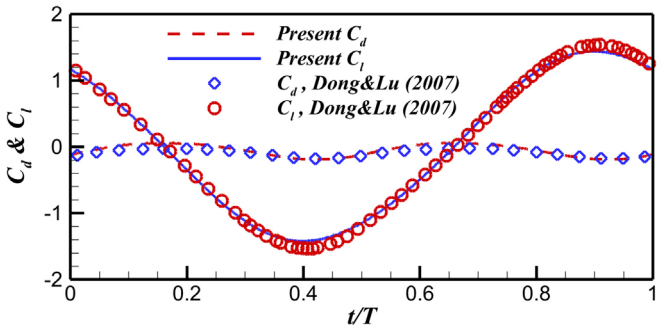


**FIG. 3.** Comparison of the drag and lift coefficient of flow over a wave foil with the previous study.

$k_b = 0.1$, $\beta = 2.9$) obtained from this study are also in excellent agreement with results from previous numerical work[40] and experimental work[41] in predicting the transverse displacement of the flag's free end, as shown in Fig. 2(b). Meanwhile, an isolated tethered wave foil in the uniform flow is simulated to ensure the capability of our solver in capturing the crucial interaction between the swimmer and fluid flow. The lift and drag force coefficient predicted by our numerical solver are in excellent agreement with the work of Dong and Lu[42] (see Fig. 3).

Grid independence studies are conducted to determine the appropriate mesh size, and it was found that a grid size of $\Delta x/c = 0.0083$ is sufficient to investigate the hydrodynamic performance of the carangiform swimmer with the caudal fin, as shown in Figs. 4(a) and 4(b). The BCF system is discretized by uniform Lagrangian points with grid spacing of $\Delta x_{solid}/c = 0.0125$. The time step independence studies are also examined, as shown in Figs. 4(c) and 4(d), and it was found that the time step $\Delta t/T = 2 \times 10^{-5}$ is enough to capture the dynamic response of the flexible structure in the BCF system.

## IV. RESULTS AND DISCUSSION

In this study, all parameters related to the BCF system are shown in Table I. Based on previous studies,[8,43] the mass ratio of $\beta = 0.2$ is a suitable value to reflect the thin nature of the caudal fin and the fin lengths of 0.2 and 0.3 times the body length of natural swimmer are adopted in this study to mimic aquatic animals, i.e., typically 0.25 for bonefish and 0.3 for milkfish.[8] The stretching ratio of $k_s = 2 \times 10^3$ is employed in all studied cases to ensure the stretching ratio of the caudal fin being less than 1%.[39] The bending stiffness $k_b$ is varied from 0.001 to 150 to study the effects of bending stiffness on the self-propulsion.

It should be pointed out that although Re adopted in this work is much lower than those of most adult swimmers, Re = 500 is close to that of larvae,[8,43–45] which is the investigated objective of the present work. In addition, the mass ratio of realistic aquatic animals should be minimal, e.g., $\beta = 0.02$. However, the present weak coupling scheme is adopted to solve the fluid–structure interaction, which triggers that a small mass ratio may induce numerical instability. Similar problem is also encountered in the work of Zhang *et al.*[46] In addition, Zhang *et al.*[47] investigated an elastic panel oscillating in a stream, and they found that the propulsive performance of the case with $\beta = 0.5$ is close to that with $\beta = 0.05$. Therefore, some inherent fluid

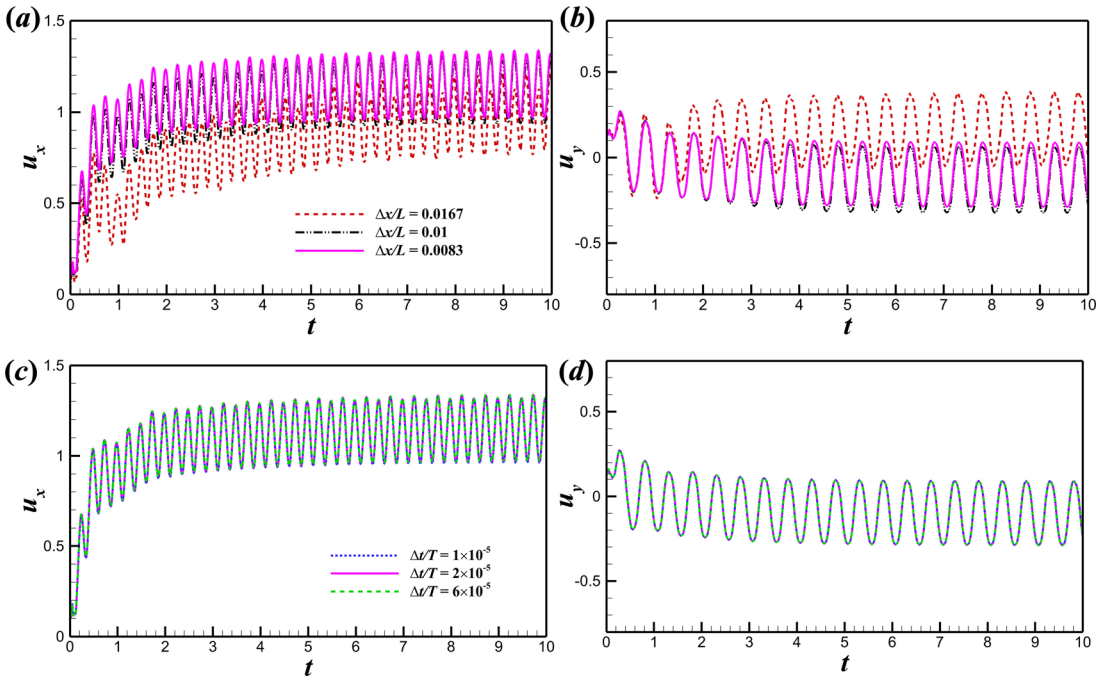


**FIG. 4.** Grid dependence studies: time histories of (a) horizontal propulsive speed and (b) vertical propulsive speed of the carangiform swimmer with the flexible caudal fin. Time dependence studies: time histories of (c) horizontal propulsive speed and (d) vertical propulsive speed. These cases are simulated with the parameters of Re = 650, $L_{fin} = 0.3$, $k_s = 2.0 \times 10^3$, $k_b = 10$, $\beta = 0.2$.

**TABLE I.** The specific values of the governing parameters applied.

| Parameters | Specifications |
|---|---|
| Re | 500 |
| Undulatory frequency, f | 2.0 |
| Stretching coefficient, $k_s$ | 2000 |
| Mass ratio, $\beta$ | 0.2 |
| Fin length, $L_{fin}$ | 0.2, 0.3 |
| Bending stiffness, $k_b$ | 0.001, 0.005, 0.01, 0.05, 0.1, 0.5, 1, 5, 10, 15, 100, 150 |

mechanisms in the self-propulsion of a carangiform swimmer with a flexible caudal fin may be revealed through cases with $\beta = 0.2$. Liu *et al.*,[43,44] Zhu *et al.*,[45] and Tian *et al.*[8] have demonstrated that the mass ratio $\beta = 0.2$ is applicable to mimic fish fins. Therefore, the mass ratio $\beta = 0.2$ is adopted to investigate the hydrodynamic performance of the BCF system.

### A. Performances of the BCF system

The BCF system with varying fin lengths from 0.2 to 0.3 at various bending stiffness values is examined through the comparison of the time-averaged propulsive speed $u_x$, propulsive efficiency $\eta$, and the hydrodynamic forces exerted on the swimmer body $F_{foil}$ and the caudal fin $F_{fin}$, as shown in Fig. 5. Among all studied cases, swimmers at small bending stiffness $k_b < 0.1$ are found to have difficulty in achieving steady forward propulsion and their propulsive efficiency is relatively low. On the other hand, the propulsive force and efficiency are enhanced at moderate bending stiffness of $0.1 \leq k_b \leq 10$ and further increasing the bending stiffness $k_b > 10$ has no effect on the propulsive force and efficiency when $L_{fin} = 0.2$. However, for longer fin length ($L_{fin} = 0.3$), further increasing the stiffness $10 < k_b \leq 100$ promotes the propulsive speed and efficiency. Nevertheless, $k_b = 100$ is the threshold limit for $L_{fin} = 0.3$ and further increasing the bending stiffness has no effect on the propulsive speed and efficiency. The time-averaged hydrodynamic forces applied on the swimmer body and caudal fin are shown in Figs. 5(c) and 5(d), respectively, indicating that there exists a propulsive pattern switching at moderate bending

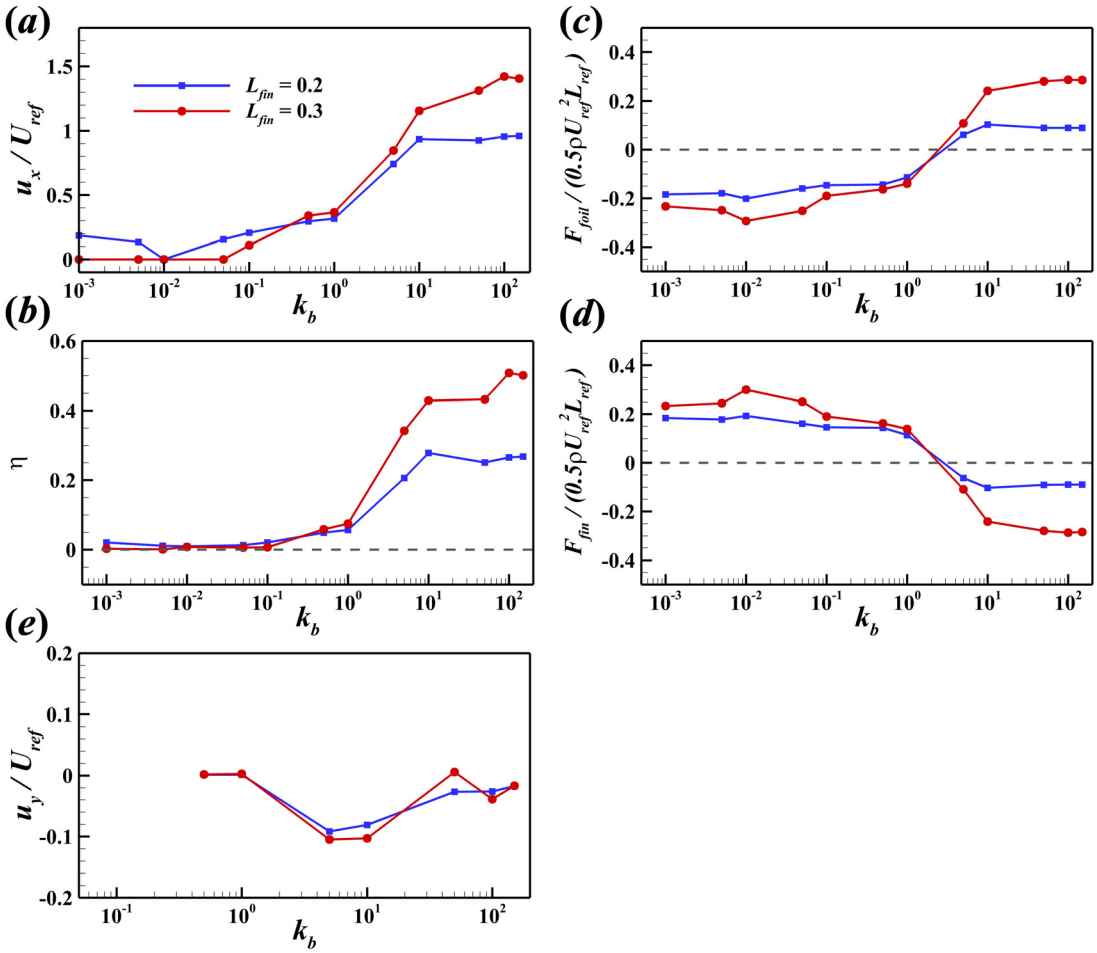


**FIG. 5.** (a) The time-averaged horizontal propulsive speed, (b) the propulsive efficiency, (c) the horizontal hydrodynamics force exerted on the wavy foil surface, (d) the horizontal hydrodynamic force exerted on the flexible caudal fin, and (e) the time-averaged lateral propulsive speed of the BCF system at different bending stiffness.

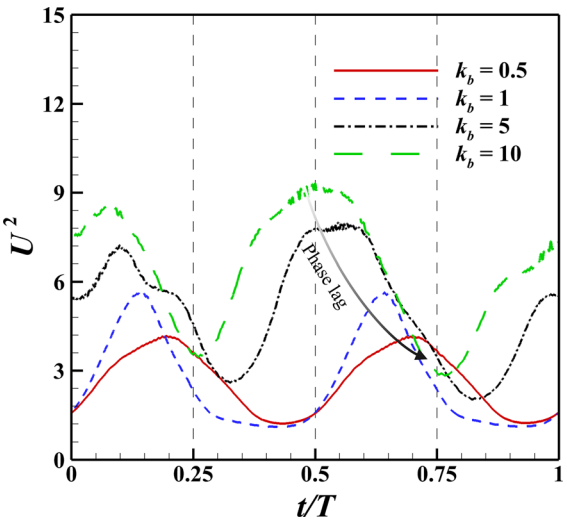


**FIG. 6.** Comparison of $U^2 = u^2 + v^2$ at the trailing edge with different bending stiffness in an undulatory period, when $L_{fin}$=0.3.

stiffness of $k_b \in (1, 5)$. For low bending stiffness ($k_b \leq 1$), the swimmer body produces thrust while the flexible caudal fin produces drag. In contrast, at $k_b \geq 5$, the flexible caudal fin plays the thrust-producing role and the swimmer body plays the drag-producing role. It should be noted that the total force exerted on the BCF system is contributed by $F_{foil}$ and $F_{fin}$; hence, the time-averaged horizontal force $F_{Hx}$ is zero at the steady propulsive stage. Since the BCF system with $L_{fin} = 0.2$ and 0.3 shows somewhat similar trends in all studied cases, the remaining sections use only the case of the BCF system at $L_{fin} = 0.3$ to avoid repetitive results. Another issue to note is that the time-averaged lateral propulsive speed $u_y$ of the BCF system at bending stiffness of $k_b \leq 0.1$ fluctuates around zero; at $0.5 \leq k_b \leq 1$, $u_y$ of the BCF system is negligible, indicating that the wake symmetry is preserved; at $k_b \geq 5$, $u_y$ of the BCF system is triggered again, which corresponds to the wake symmetry breaking discussed in Sec. IV B.

To elucidate the enhancement of propulsive speed and propulsive efficiency induced by the caudal fin's bending stiffness, the flapping velocity at the trailing edge is examined. Here, we directly compared the square of the trailing flapping velocity, which is associated with the kinematic energy of wake flow, because large wake flow energy is able to provide enhanced reaction momentum, promoting the thrust of the BCF system. It is evident from Fig. 6 that $U^2$ of the trailing edge is proportional to the propulsive speed and $U^2$ at $k_b = 5$ and 10 is significantly larger than that of cases at $k_b = 0.5$ and 1. Moreover, the flexibility induced the wave lag phase can been observed in Fig. 6.

## B. Flow structures

The propulsive performance of the BCF system is closely associated with the flow structure; hence, the vortical structures and pressure distribution around the BCF system, as well as the time-averaged horizontal velocity field, are explored. The wake vortical structures (see Fig. 7) of BCF systems at different bending stiffness show that there are two vortex patterns formed in the wake flow: (i) a typical reverse Bénard–von Kármán vortex configuration at bending stiffness $0.5 \leq k_b \leq 1$ and (ii) a deflected reverse Bénard–von Kármán wake with the secondary vortex street at bending stiffness $k_b \geq 5$. Details on the generation of asymmetric deflected rBvK would be discussed in the following section. It should be noted that the BCF system cannot reach a steady propulsive stage with a chaotic vortex street at $k_b \leq 0.1$. The switching of wake vortex patterns corresponds to the switching of drag-production part and thrust-production part reported in Sec. IV A, which demonstrates that the vortex street is closely associated with the hydrodynamic force. The hydrodynamic force exerted on the BCF system can be decomposed into friction force and pressure force. Dong and Lu[42] reported that the friction drag exerted on the undulatory swimmer is almost constant in one oscillation period; thus, the propulsive behavior is dominated by the surface pressure distribution. Therefore, the pressure field around BCF systems at $k_b = 1$ and 5 is further analyzed to investigate the mechanism behind the thrust-drag switch at $L_{fin} = 0.3$.

The pressure distributions and corresponding force evolutions of BCF systems at $k_b = 1$ and 5 over the first-half propulsive period are shown in Fig. 8. The snapshots of pressure contours shown in Figs. 8(a)

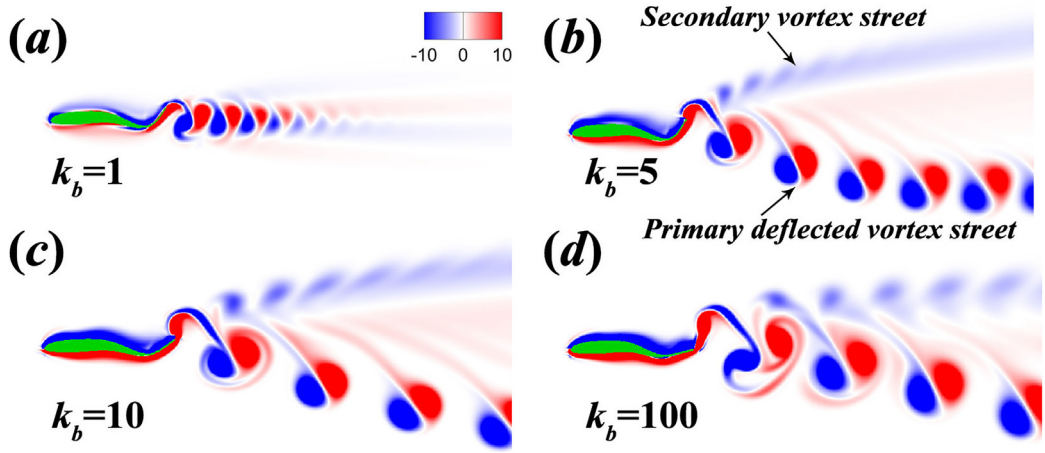


**FIG. 7.** The instantaneous vorticity field of the BCF system at (a) $k_b = 1$, (b) $k_b = 5$, (c) $k_b = 10$, and (d) $k_b = 100$, when $L_{fin} = 0.3$.

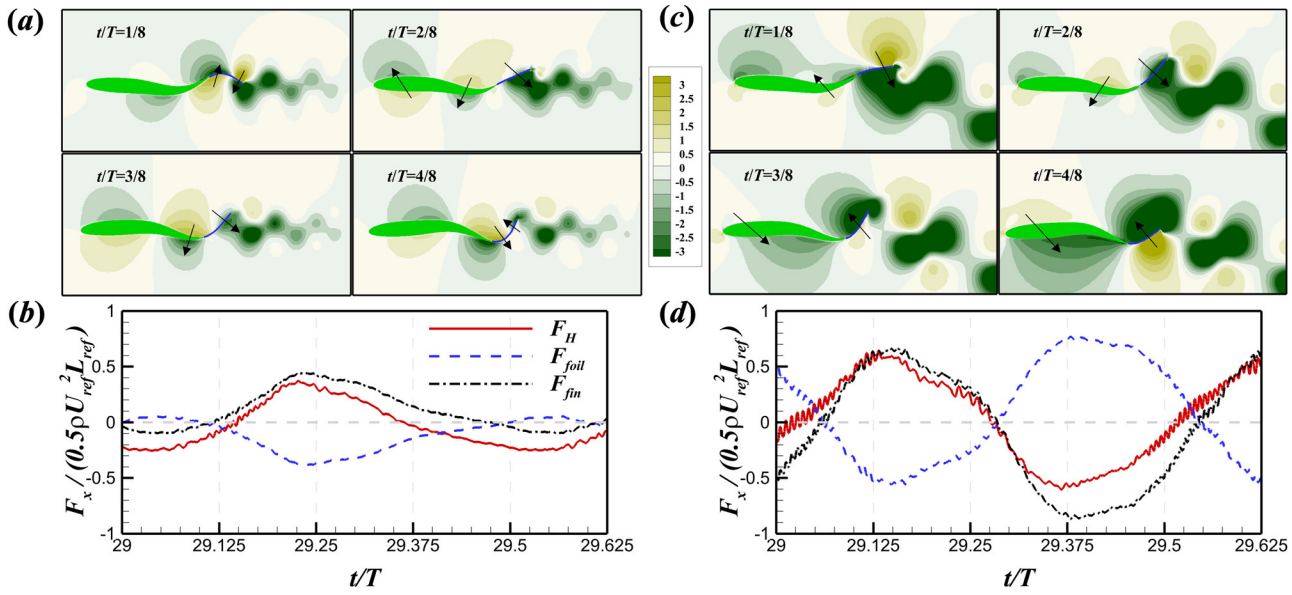


**FIG. 8.** (a) and (c) The pressure distribution around the BCF system at $k_b = 1$ and $k_b = 5$ during the first-half propulsive period, respectively. (b) and (d) The evolutions of corresponding horizontal forces. It should be noted that $F_{foil}$ mentioned here do not have the inertia force component.

and 8(c) for $k_b = 1$ and $k_b = 5$, respectively, are the key to explain the observed thrust-drag switch in BCF systems. A close examination of Fig. 8(a) for $k_b = 1$ led to the following observations: At $t/T = 1/8$, an anti-symmetric pressure distribution is formed along the caudal fin, balancing the force along the flexible caudal fin, which led to $F_{fin} \approx 0$ at this instance. At $t/T = 2/8$, a positive pressure region and a negative pressure region appear at the top and bottom of the caudal fin as a result of the unfavorable position of the caudal fin, resulting in a drag force being developed along the caudal fin and led to a positive $F_{fin}$ at this instance. In addition, the pressure difference between the sides of the swimmer's body resulted in a thrust force being applied on the swimmer surface. At $t/T = 3/8$, the caudal fin experiences a similar pressure field as of $t/T = 2/8$, generating a drag force over the caudal fin and yielding a negative value of $F_{fin}$. In addition, the pressure force generated by pressure difference is almost vertical resulting the decrease in thrust force exerted on the swimmer's body. At $t/T = 4/8$, an anti-symmetric pressure distribution is formed again over the caudal fin, which led to $F_{fin} \approx 0$ at this particular instance.

A close examination of Fig. 8(c) for $k_b = 5$ led to the following observations: At $t/T = 1/8$ and 2/8, a positive pressure area and a negative pressure area are formed at the top and bottom of the caudal fin due to the caudal fin locating at the unfavorable position, resulting in the formation of a drag force over the flexible fin, yielding a positive value in $F_{fin}$, as shown in Fig. 8(d). On the other hand, the pressure distribution on the swimmer surface provides a thrust force, yielding a negative $F_{foil}$. At $t/T = 3/8$ and 4/8, there is a positive region formed at the bottom of the caudal fin due to the favorable position of the caudal fin, resulting in the generation of thrust force over the caudal fin, which led to a negative $F_{foil}$. However, the positive pressure region at the top of the swimmer generates a drag force on the swimmer body.

It is evident from Fig. 7 that the wake symmetry breaking can be either inhibited or triggered. To understand how the flexibility of the caudal fin affects the wake symmetry, the velocity profiles along the caudal fin at different bending stiffness are shown in Fig. 9. It can be observed that the lateral trailing edge velocity is promoted as the bending stiffness increases, and the newly generated vortices shed from the

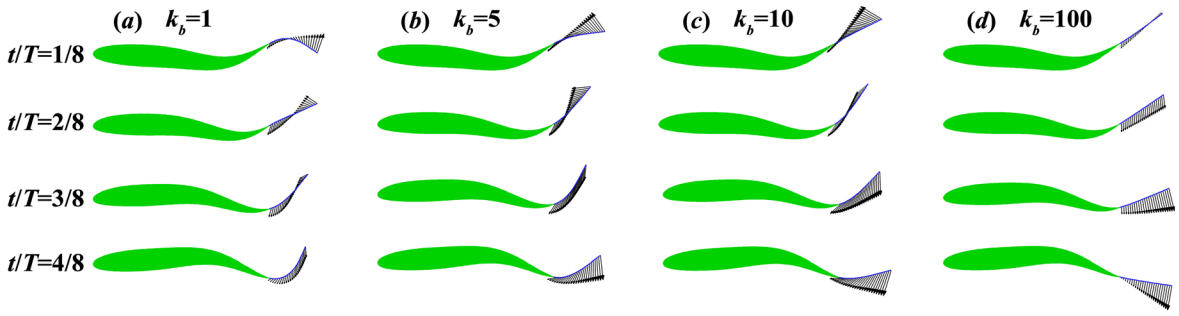


**FIG. 9.** The velocity profile along the flexible caudal fin at (a) $k_b = 1$, (b) $k_b = 5$, (c) $k_b = 10$, and (d) $k_b = 100$ during the first-half propulsive period.

caudal fin's trailing edge result in a relatively high lateral phase speed, which is the key component to break the balance between the adjacent vortices,[13] causing the wake symmetry breaking. Shinde and Arakeri[18] found that the point of zero velocity (PoZV) over the caudal fin is a "moving hinge point" related to the vortex generation, and a newly generated vortex is shed from the flexible fin as the PoZV arrives the trailing edge. In the present simulations, it is observed that, with the increasing in the bending stiffness, the moving speed of the PoZV over the caudal fin is enhanced, promoting the vortex generation speed, which explains the phase lag observed between the vortex streets at different bending stiffness (see Fig. 7).

The PoZV separates the caudal fin into an active portion and a passive portion.[18] With the build-in supported condition, the motion of active portion depends on the undulatory foil and moves the surrounding flow, which is the main component to accelerate the wake flow to form the jet structure. On the other hand, the motion of the passive portion is dominated by the ambient flow, extracting energy form fluid, which is normally related to the vortex shedding position. Figure 9 shows that the active portion occupies more region of the caudal fin in a whole period as the bending stiffness increases, indicating that the wake flow extracted more energy from the BCF system at high bending stiffness condition to generate more thrust on the system, explaining the observed increase in propulsive speed under the higher bending stiffness condition.

The time-averaged horizontal velocity field and the corresponding velocity vector field at different bending stiffness are shown in Fig. 10. The symmetric jet transits to irregular asymmetric jet as the bending stiffness increases, resulting from the enhanced lateral flapping velocity at the trailing edge (see also Fig. 9). In addition, there is a fluid region with large forward velocity at the top of the deflected jet structure. Liu *et al.*[43] reported that the wake symmetry affects propulsive performance, because the backward momentum of the asymmetric jet cannot be fully transformed into thrust force. In the present simulations, the observed increase in propulsive efficiency under the high bending stiffness condition is associated with the fact that the BCF system can effectively promote flapping velocity of the trailing edge and transfer energy to the wake flow as bending stiffness increases. The flow generation mechanism can be clearly observed in the time-averaged velocity vector field. The flapping motion of the caudal fin causes the fluid to be drawn from quiescent ambience into the flapping area of the flexible fin, thereby accelerating the flow at the downstream to create the coherent jet, which echoed the study of Shinde and Arakeri.[18] It should be noted that, at $k_b = 5$, the fluid drawn by the caudal fin mostly comes from the top area of the inclined jet formed by the secondary vortex street.

## C. Vortex generation mechanism

As previously described, the deflected rBvK with a secondary vortex street is observed at $k_b \geq 5$. Here, the vortex generation mechanism is investigated in detail through the visual inspection of Fig. 11. At $t = T/8$, a newly formed clockwise vortex C1 is generated at the trailing edge. Subsequently, a strong strain area is created between C1, the trailing edge and the secondary vortex street due to the caudal fin continuously flapping up and the induced velocity generated by the secondary vortex street, resulting in the separation of C1 due to stretch into C1 and C2 at $t = 4T/8$, forming the secondary vortex street. As the trailing edge flaps downward, a vortex C3 with the opposite sign emerges over the preceding vortex C1. With $u_y = -0.1$, the vortical strength of C3 is further enhanced, contributing to the imbalance between the two opposite sign vortices and a dipolar structure is formed. The primary vortex and the secondary vortex generate induced velocities on C3 respectively; hence, C3 is stretched by the primary vortex street and secondary vortex street. Resulting from the larger vortical strength of the primary wake, C3 is pulled into the primary wake inducing a strong strain between C3 and the secondary vortex street, thereby stretching C3 into C3 and C4. However, the vortical strength of C4 is weak and it dissipates rapidly.

To better understand the spatial-temporal feature of different propulsive patterns as well as to elucidate the mechanism of the bending stiffness effect, dynamic mode decomposition (DMD) is adopted to analyze the flow field at $k_b = 1$ and $k_b = 5$. Readers are referred to

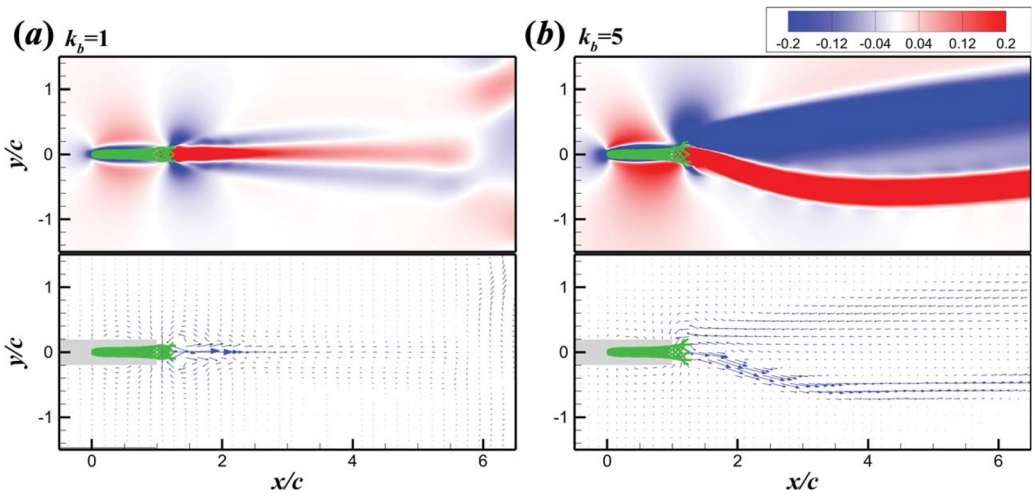


**FIG. 10.** The time-averaged horizontal velocity field and the corresponding velocity vector field at (a) $k_b = 1$ and (b) $k_b = 5$.

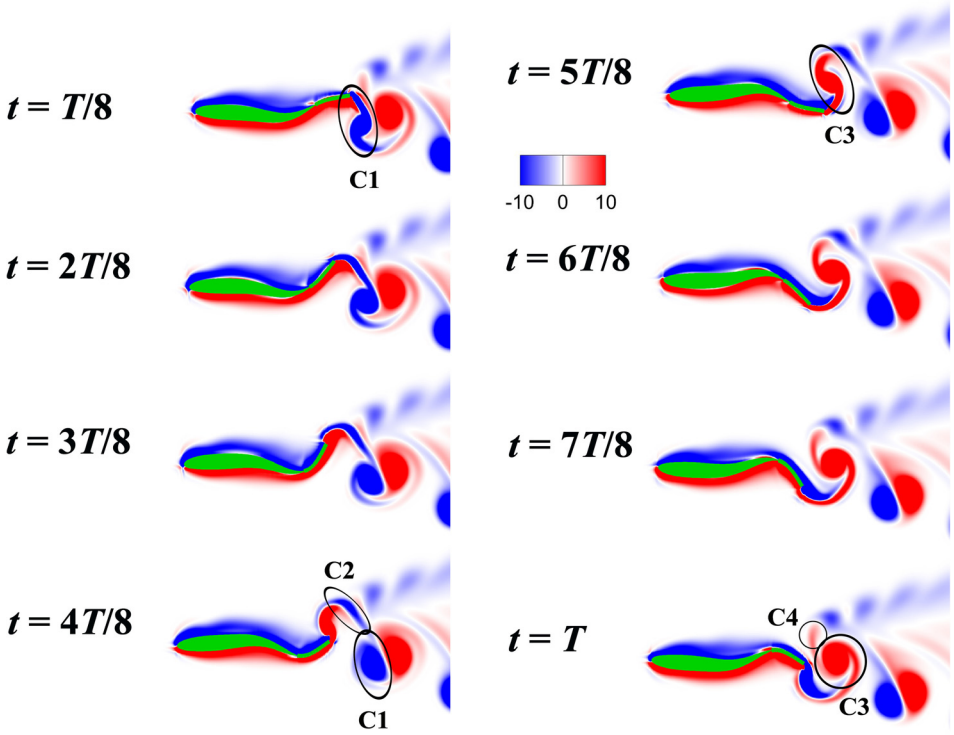


FIG. 11. Vortex generation of the deflected primary vortex street and secondary vortex street.

previous works[48,49] for detailed information on the DMD algorithm. In this study, the velocity field in the wake region of $6c \times 5c$ is further scrutinized using the DMD analysis, which is close to the trailing edge of the caudal fin. It should be noted that the DMD region has translational motions and its velocity is set the same as that of the BCF system. The energy distributions of the DMD velocity modes at $k_b = 1$ and $k_b = 5$ are shown in Fig. 12, and the modal amplitude $\phi$ denotes the relative energy of the mode as well as its importance; thus, it can be adopted as a selection criterion for dominant modes. The dominant modes for the BCF systems are mode M1 ($f_{M1} = 0$ corresponds to averaged flow field), mode M2 ($f_{M2} = 2$ corresponds to the excited frequency resonant flow field) and other superharmonic modes of mode M2. Therefore, mode M2 is adopted to characterize the main feature of the flow field.

A closer examination of the horizontal velocity at mode M2 for $k_b = 1$ echoed our initial finding that this BCF system has the regular rBvK vortex configuration and each vortex in the vorticity mode M2 [see Fig. 13(b)] denotes two opposite velocity regions in the horizontal velocity mode M2 [see Fig. 13(a)]. In contrast, the staggered vortices with the opposite rotation direction [see Fig. 13(d)] is observed for $k_b = 5$, indicating a deflected rBvK vortex street with twisted velocity staggered strips. It should be noted that there are some small staggered vortices corresponding to the secondary vortex street and the positive vortex in the secondary vortex street maintains proper spacing among the negative vortices and dissipates rapidly. This explains why the secondary vortex street is composed of negative vortices. In addition, the inherent frequency of the secondary street is the same as the undulatory frequency, which quantitatively confirms the explanation of Bose *et al.*[50]

## V. CONCLUDING REMARKS

The hydrodynamic performance of a self-propelled undulatory swimmer with a flexible caudal fin (BCF system) in the absence of a free stream is investigated numerically. The effect of bending stiffness is examined with the caudal fin length of 0.2 and 0.3.

Based on the hydrodynamic performance, i.e., propulsive speed $u_x$ and propulsive efficiency $\eta$, the bending stiffness can be divided into three groups: small bending stiffness $k_b < 0.1$, moderate bending stiffness $0.1 \leq k_b \leq 10$, and large bending stiffness $k_b > 10$. At small bending stiffness, the BCF system cannot achieve a steady forward propulsion and the propulsive efficiency is relatively low; at moderate bending stiffness, the propulsive speed and efficiency are promoted with an increase in bending stiffness; and at large bending stiffness, the effects of bending stiffness are negligible for $L_{fin} = 0.2$, but the propulsive speed and efficiency are slightly promoted as the bending stiffness increases for $L_{fin} = 0.3$. The switch between the drag and thrust production occurred in $k_b \in (1, 5)$. In the tethered BCF model,[8] the time-averaged hydrodynamic forces show a similar trend to that of the present work, where the caudal fin changes from a drag generator to a thrust generator with the increase in bending stiffness. However, it should be noted that the switching for the tethered BCF model is triggered at a minimal bending stiffness $k_b \approx 0.1$, which differs from that of the unconstrained BCF model.

The wake street of the BCF system is the rBvK vortex configuration, and the deflection of the vortex street starts to form at large bending stiffness. The thrust and drag generations are analyzed through the evolutions of pressure field. The evolutions of the velocity profile along the caudal fin reveal that the moving speed of PoZV is further

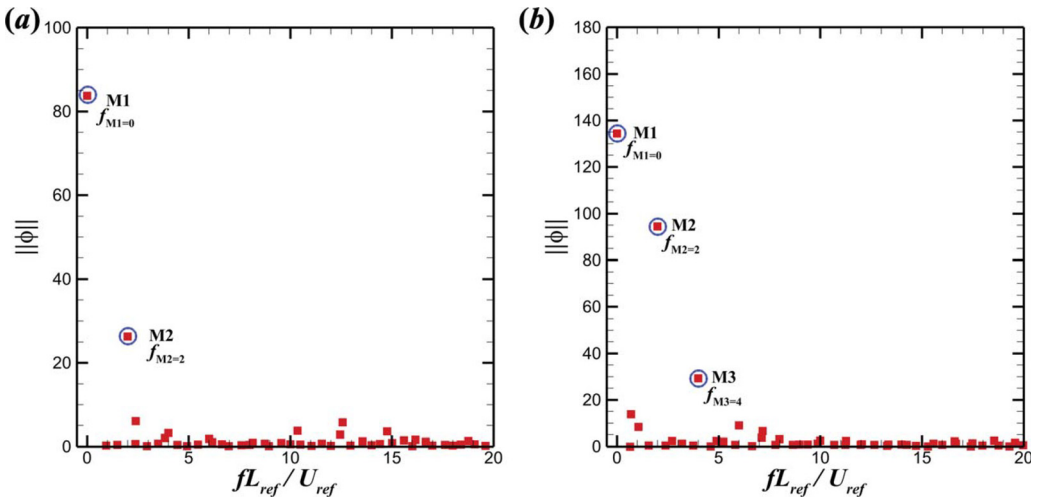


**FIG. 12.** Energy distribution of the DMD modes in the frequency domain at (a) $k_b = 1$ and (b) $k_b = 5$.

enhanced as the bending stiffness increases, promoting the speed of vortex generation. As the bending stiffness increases, the active portion occupies more region of the caudal fin in one undulatory period, providing the wake flow with more kinetic energy. Furthermore, the time-averaged horizontal velocity and velocity vector field show that the orderly jet and the deflected jet are formed in the rBvK and the deflected rBvK, respectively, and the strength of backward jet is related to the thrust generation. Moreover, the velocity vector field reveals the flow generation mechanism, where it draws quiescent ambient fluid into the caudal fin flapping area and pushing it toward the downstream. There is a two-layered vortex street at $k_b = 0.01$ in the tethered BCF model,[8] while it does not appear in the unconstrained BCF model. Because, in the unconstrained BCF system, the flexible fin with such small bending stiffness bends excessively, enhancing the horizontal oscillation; thus, it is hard to achieve a stable propulsive state.

In addition, the vortex generation mechanism reveals that the deflected rBvK is generated by the imbalance of two adjacent vortices' vortical strength, and a secondary vortex street is formed by the large strain between the primary vortex street and the secondary vortex street. Moreover, the DMD analysis reveals that the excited frequency resonant is the main component of the flow field and the inherent

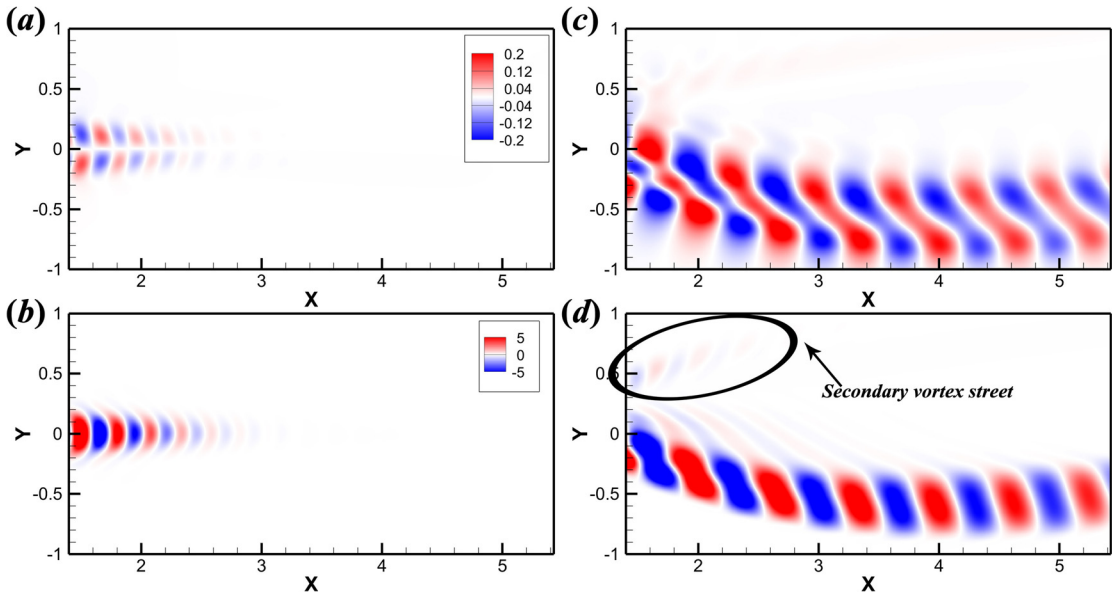


**FIG. 13.** (a) The horizontal velocity and (b) the vorticity field for mode M2 of the BCF system at $k_b = 1$; (c) the horizontal velocity and (d) the vorticity field for mode M2 of the BCF system at $k_b = 5$.

frequency of the secondary vortex street correlates well with the undulatory frequency.

The results of this study are carefully scrutinized to elucidate how the flexibility of the caudal fin affects the hydrodynamic performance of self-propelled carangiform in the absence of a free stream, providing some inspirations to optimize the design of AUVs. However, more works are warranted to include other important effects such as the three-dimensional geometry of the caudal fin and the mass ratio of flexible fin, inclusive of more propulsive parameters, and varying Reynolds numbers to better mimic the realistic biology system. Nevertheless, these will be the subject of our future work.

## ACKNOWLEDGMENTS

This work has been supported by the Department of Science and Technology of Guangdong Province (Grant No. 2020B1212030001), the Key-Area Research and Development Program of Guangdong Province (Grant No.2021B0101190003), and the Shenzhen Science and Technology Program (Grant No. KQTD20180411143441009). Numerical simulations have been supported by the Center for Computational Science and Engineering of Southern University of Science and Technology.

## AUTHOR DECLARATIONS

### Conflict of Interest

The author has no conflicts to disclose.

## DATA AVAILABILITY

The data that support the findings of this study are available from the corresponding authors upon reasonable request.

## REFERENCES

[1]M. Triantafyllou, G. S. Triantafyllou, and D. K. P. Yue, "Hydrodynamics of fishlike swimming," Annu. Rev. Fluid Mech. **32**(1), 33–53 (2000).
[2]M. S. U. Khalid, J. Wang, I. Akhtar, H. Dong, M. Liu, and A. Hemmati, "Why do anguilliform swimmers perform undulation with wavelengths shorter than their bodylengths?," Phys. Fluids **33**(3), 031911 (2021).
[3]M. S. U. Khalid, J. Wang, H. Dong, and M. Liu, "Flow transitions and mapping for undulating swimmers," Phys. Rev. Fluids **5**(6), 063104 (2020).
[4]M. S. U. Khalid, J. Wang, I. Akhtar, H. Dong, M. Liu, and A. Hemmati, "Larger wavelengths suit hydrodynamics of carangiform swimmers," Phys. Rev. Fluids **6**(7), 073101 (2021).
[5]C.-Y. Guo, Y.-F. Kuai, Y. Han, P. Xu, Y.-W. Fan, and C.-D. Yu, "Hydrodynamic analysis of propulsion process of zebrafish," Phys. Fluids **34**(2), 021910 (2022).
[6]G. Lauder, "Fish locomotion: Recent advances and new directions," Annu. Rev. Marine Sci. **7**, 521–545 (2015).
[7]M. Sfakiotakis, D. Lane, J. Bruce, and C. Davies, "Review of fish swimming modes for aquatic locomotion," IEEE J. Ocean. Eng. **24**(2), 237–252 (1999).
[8]L. Tian, Z. Zhao, W. Wang, and N. Liu, "Length and stiffness effects of the attached flexible plate on the flow over a traveling wavy foil," Acta Mech. Sin. **37**, 1404–1412 (2021).
[9]S. Gupta, N. Thekkethil, A. Agrawal, K. Hourigan, M. Thompson, and A. Sharma, "Body-caudal fin fish-inspired self-propulsion study on burst-and-coast and continuous swimming of a hydrofoil model," Phys. Fluids **33**(9), 091905 (2021).
[10]N. Thekkethil, A. Sharma, and A. Agrawal, "Unified hydrodynamics study for various types of fishes-like undulating rigid hydrofoil in a free stream flow," Phys. Fluids **30**(7), 077107 (2018).
[11]T. Yao-Tsu Wu, "Hydromechanics of swimming propulsion. Part 1. Swimming of a two-dimensional flexible plate at variable forward speeds in an inviscid fluid," J. Fluid Mech. **46**(2), 337–355 (1971).
[12]J. Katz and D. Weihs, "Hydrodynamic propulsion by large amplitude oscillation of an airfoil with chordwise flexibility," J. Fluid Mech. **88**(3), 485–497 (1978).
[13]B. Wu, C. Shu, M. Wan, Y. Wang, and S. Chen, "Hydrodynamic performance of an unconstrained flapping swimmer with flexible fin: A numerical study," Phys. Fluids **34**(1), 011901 (2022).
[14]S. Heathcote and I. Gursul, "Flexible flapping airfoil propulsion at low Reynolds numbers," AIAA J. **45**(5), 1066–1079 (2007).
[15]P. Dewey, B. Boschitsch, K. Moored, H. Stone, and A. Smits, "Scaling laws for the thrust production of flexible pitching panels," J. Fluid Mech. **732**, 29 (2013).
[16]S. Shinde and J. Arakeri, "Flexibility in flapping foil suppresses meandering of induced jet in absence of free stream," J. Fluid Mech. **757**, 231 (2014).
[17]M. J. David, R. N. Govardhan, and J. H. Arakeri, "Thrust generation from pitching foils with flexible trailing edge flaps," J. Fluid Mech. **828**, 70 (2017).
[18]S. Shinde and J. Arakeri, "Physics of unsteady thrust and flow generation by a flexible surface flapping in the absence of a free stream," Proc. R. Soc. A **474** (2218), 20180519 (2018).
[19]M. Kurt, A. Mivehchi, and K. Moored, "High-efficiency can be achieved for non-uniformly flexible pitching hydrofoils via tailored collective interactions," Fluids **6**(7), 233 (2021).
[20]N. Liu, Y. Peng, Y. Liang, and X. Lu, "Flow over a traveling wavy foil with a passively flapping flat plate," Phys. Rev. E **85**(5), 056316 (2012).
[21]N. Liu, Y. Peng, and X. Lu, "Length effects of a built-in flapping flat plate on the flow over a traveling wavy foil," Phys. Rev. E **89**(6), 063019 (2014).
[22]A. K. Kancharala and M. K. Philen, "Study of flexible fin and compliant joint stiffness on propulsive performance: Theory and experiments," Bioinspiration Biomimetics **9**(3), 036011 (2014).
[23]M. Bergmann, A. Iollo, and R. Mittal, "Effect of caudal fin flexibility on the propulsive efficiency of a fish-like swimmer," Bioinspiration Biomimetics **9**(4), 046001 (2014).
[24]Z. Zhao and L. Dou, "Effects of the structural relationships between the fish body and caudal fin on the propulsive performance of fish," Ocean Eng. **186**, 106117 (2019).
[25]A. Gao and M. Triantafyllou, "Independent caudal fin actuation enables high energy extraction and control in two-dimensional fish-like group swimming," J. Fluid Mech. **850**, 304–335 (2018).
[26]S. Reddy, S. Sen, and C. Har, "Effect of flexural stiffness distribution of a fin on propulsion performance," Mech. Mach. Theory **129**, 218–231 (2018).
[27]J. Alaminos-Quesada and R. Fernandez-Feria, "Propulsion of a foil undergoing a flapping undulatory motion from the impulse theory in the linear potential limit," J. Fluid Mech. **883**, A19 (2020).
[28]X. He, Q. Guo, and J. Wang, "Extended flexible trailing-edge on the flow structures of an airfoil at high angle of attack," Exp. Fluids **60**(8), 1–22 (2019).
[29]D. Zhang, G. Pan, L. Chao, and Y. Zhang, "Effects of Reynolds number and thickness on an undulatory self-propelled foil," Phys. Fluids **30**(7), 071902 (2018).
[30]X. Zhao, Z. Chen, L. Yang, N. Liu, and C. Shu, "Efficient boundary condition-enforced immersed boundary method for incompressible flows with moving boundaries," J. Comput. Phys. **441**, 110425 (2021).
[31]W.-X. Huang, S. J. Shin, and H. J. Sung, "Simulation of flexible filaments in a uniform flow by the immersed boundary method," J. Comput. Phys. **226**(2), 2206–2228 (2007).
[32]J. Ma, Z. Wang, J. Young, J. Lai, Y. Sui, and F.-B. Tian, "An immersed boundary-lattice Boltzmann method for fluid-structure interaction problems involving viscoelastic fluids and complex geometries," J. Comput. Phys. **415**, 109487 (2020).
[33]C. Shu, Y. Wang, C. J. Teo, and J. Wu, "Development of lattice Boltzmann flux solver for simulation of incompressible flows," Adv. Appl. Math. Mech. **6**(4), 436–460 (2014).
[34]Y. Wang, C. Shu, C. J. Teo, and J. Wu, "An immersed boundary-lattice Boltzmann flux solver and its applications to fluid–structure interaction problems," J. Fluids Struct. **54**, 440–465 (2015).
[35]F.-B. Tian, H. Luo, J. Song, and X.-Y. Lu, "Force production and asymmetric deformation of a flexible flapping wing in forward flight," J. Fluids Struct. **36**, 149–161 (2013).
[36]F.-B. Tian, H. Dai, H. Luo, J. Doyle, and B. Rousseau, "Fluid–structure interaction involving large deformations: 3D simulations and applications to biological systems," J. Comput. Phys. **258**, 451–469 (2014).

[37]J. Wu, C. Shu, N. Zhao, and F.-B. Tian, "Numerical study on the power extraction performance of a flapping foil with a flexible tail," Phys. Fluids **27**(1), 013602 (2015).
[38]L. Kang, W. Cui, X.-Y. Lu, and H. Huang, "Hydrodynamic force induced by vortex–body interactions in orderly formations of flapping tandem flexible plates," Phys. Fluids **34**(2), 021901 (2022).
[39]H.-Z. Yuan, X.-D. Niu, S. Shu, M. Li, and H. Yamaguchi, "A momentum exchange-based immersed boundary-lattice Boltzmann method for simulating a flexible filament in an incompressible flow," Comput. Math. Appl. **67**(5), 1039–1056 (2014).
[40]M. de Tullio and G. Pascazio, "A moving-least-squares immersed boundary method for simulating the fluid–structure interaction of elastic bodies with arbitrary thickness," J. Comput. Phys. **325**, 201–225 (2016).
[41]D. Kim, J. Cossé, C. Cerdeira, and M. Gharib, "Flapping dynamics of an inverted flag," J. Fluid Mech. **736**, R1 (2013).
[42]G.-J. Dong and X.-Y. Lu, "Characteristics of flow over traveling wavy foils in a side-by-side arrangement," Phys. Fluids **19**(5), 057107 (2007).
[43]K. Liu, H. Huang, and X.-Y. Lu, "Hydrodynamic benefits of intermittent locomotion of a self-propelled flapping plate," Phys. Rev. E **102**(5), 053106 (2020).
[44]K. Liu, X. Liu, and H. Huang, "Scaling the self-propulsive performance of pitching and heaving flexible plates," J. Fluid Mech. **936**, A9 (2022).
[45]X. Zhu, G. He, and X. Zhang, "Flow-mediated interactions between two self-propelled flapping filaments in tandem configuration," Phys. Rev. Lett. **113**(23), 238105 (2014).
[46]C. Zhang, H. Huang, and X.-Y. Lu, "Effect of trailing-edge shape on the self-propulsive performance of heaving flexible plates," J. Fluid Mech. **887**, A7 (2020).
[47]Y. Zhang, C. Zhou, and H. Luo, "Effect of mass ratio on thrust production of an elastic panel pitching or heaving near resonance," J. Fluids Struct. **74**, 385–400 (2017).
[48]P. Schmid, "Dynamic mode decomposition of numerical and experimental data," J. Fluid Mech. **656**, 5–28 (2010).
[49]Q. Zheng and M. Mahbub Alam, "Evolution of the wake of three inline square prisms," Phys. Rev. Fluids **4**(10), 104701 (2019).
[50]C. Bose, S. Gupta, and S. Sarkar, "Dynamic interlinking between near-and far-field wakes behind a pitching–heaving airfoil," J. Fluid Mech. **911**, A31 (2021).